Research Article

Min Song*, M. Sukumar, C. S. K. Raju, S. V. K. Varma, M. Ijaz Khan, Fuad A. Awwad, and Emad A. A. Ismail

Inspection of Couette and pressure-driven Poiseuille entropy-optimized dissipated flow in a suction/injection horizontal channel: Analytical solutions

https://doi.org/10.1515/phys-2023-0109
received March 22, 2023; accepted August 21, 2023

Abstract: The main aim of this study is to analyse the electrically conductive flow of compressible liquids by two infinitely permeable surfaces. The distance between the two surfaces is h. Thermal relation consists of viscous dissipation. The entropy features along with magnetic force and dissipation are taken into account. The x-axis extends in the flow path along the bottom stationary plate, whereas the y-axis is orthogonal to the surfaces. The channel plates are subjected to a consistent transverse magnetic field that is implemented perpendicularly. Herein, two scenarios are investigated: the first is the Couette flow, and in the second scenario, both porous surfaces are parallel and fixed at a distance of $2h$, and the motion is a Poiseuille flow controlled by pressure. The flow across the x-axis is supposed to be generated and dependent on y exclusively. The governed system is solved using analytical solutions. It is found that the entropy formation is higher near the cloud porous plate in comparison to the hot porous plate and the increasing values of the suction/injection parameter increase the fluid temperature. The increase in the magnetic field parameter decreases the momentum boundary layer thickness. The Brinkman number improves the thermal boundary thickness. The magnetic field parameter, suction/injection, and the Brinkman number accelerate the entropy formation in both cases.

Keywords: analytical solution, viscous dissipation, suction/injection, MHD, horizontal channels and entropy formation

*** Corresponding author: Min Song,** The International Office, Shandong Technology and Business University, Yantai 264005, China, e-mail: minsongyt@163.com
M. Sukumar: Department of Mathematics, Dr. SRK Govt. Arts College (Pondicherry University), Yanam – 533464, UT of Puducherry, India
C. S. K. Raju: Department of Mathematics, GITAM School of Science, GITAM Deemed to be University, Bangalore Campus – Karnataka, 562163, Bangalore, India
S. V. K. Varma: Department of Mathematics, REVA University, Bangalore, India
M. Ijaz Khan: Department of Mathematics and Statistics, Riphah International University, I-14, Islamabad 44000, Pakistan; Department of Mechanical Engineering, Lebanese American University, Kraytem, Beirut, Lebanon
Fuad A. Awwad, Emad A. A. Ismail: Department of Quantitative analysis, College of Business Administration, King Saud University, P.O. Box 71115, Riyadh 11587, Saudi Arabia

Nomenclature

B_0	magnetic of strength
Br	Brinkman number
C_p	specific heat at constant pressure
Ec	Eckert number
M	magnetic field parameter
N_f	fluid friction irreversibility
N_m	Joule heating irreversibility
N_s	total entropy rate
N_t	thermal transport irreversibility
Pr	Prandtl number
S	dimensionless suction/injection velocity
T	fluid temperature
T_0	temperature at the lower plate
T_w	temperature at the upper plate
U	porous plate uniform velocity
ν	kinematic viscosity
v_0	velocity of suction/injection
v	fluid velocity
σ	electrical conductivity of the fluid
ρ	fluid density
Ω	temperature difference variable

1 Introduction

One of the fundamental processes in computational fluid dynamics is the Couette and Poiseuille flow, in which the flow pattern is caused by the motion of the boundary surface. The generalised circulation of a viscous incompressible flow is created by a plate travelling similarly to a stationary plate and facilitated by favourable pressure gradient conditions. The Couette flow is valuable for a plethora of engineering purposes and is thoroughly investigated from both mechanics and heat transmission viewpoints. Muhuri [1] investigated the Couette interaction between two porosity surfaces where one of the surfaces travels at a uniform speed with suction/injection. Because of their plethora of engineering and commercial uses, the hydro-magnetic link tends to flow and has attracted the interest of many scientists. These streams can be discovered in magnetohydrodynamics (MHD) generators, geothermal underground aquifers, petroleum storage tanks, business incubators, and micro-liquid instruments. Multiple scholars [2–7] have examined MHD fluid flow in a variety of physical settings.

Due to the formation of entropy, the majority of commercial and scientific flow processes and thermodynamic frameworks cannot function at ideal levels. Consequently, it is essential to identify the causes of entropy formation in order to mitigate their consequences and maximise the flow's performance. Numerous academics have theorised the formation of entropy in heat flow regimes under various physical conditions [8–10]. Makinde and Eegunjobi [11] published a numerical result for the impacts of convective heating on entropy formation in a permeable-walled channel. Eegunjobi and Makinde [12] analysed the MHD stream flow having porous walls and convective heating. Zhao *et al.* [13], Dai *et al.* [14], and Xu *et al.* [15] worked on high-efficiency sub-microscale uncertainty measurements, ultra-wideband branch waveguide coupler with low-amplitude imbalances, and dual-mode on-chip band-pass filters, respectively. The pathways of energy relaxation of hot electrons and the effect of rotation rate and current speed are examined by Du *et al.* [16] and Wang *et al.* [17]. A few discussions in this direction are presented in previous studies [18–20].

The pressure-driven Poiseuille flow refers to the flow of a viscous, incompressible fluid that is produced by two parallel porosity plates that are $2h$ apart and fixed. None of the previous discussions on radioactive magnetohydrodynamics porous channels examined the irreversibility in the light of entropy production. A number of scientists [21–24] have studied the MHD flow and thermal performance across porous media in the presence of radiation under different settings. Kumar *et al.* [25] investigated the formation of entropy in a Poiseuille flow across a partly porous material-filled conduit. Chauhan and Khemchandani [26] described entropy development in the Poiseuille flow of a temperature-dependent viscosity liquid through a tube with a typically porous wall with radiant energy. Das and Jana [27] examined the entropy formation in a magnetohydrodynamic porous medium with a continuous pressure gradient. Vyas and Rai [28] examined the entropy domain for a radiative MHD Couette flow inside a channel with a typically porous substrate.

The main aim of this study is to analyse the electrically conducting flow of the compressible fluid subject to two infinitely porous surfaces. The distance between the two plates is h. The thermal relation in the presence of a dissipation effect is discussed. The physical features of the entropy rate along with the magnetic force and dissipation are addressed. The magnetic force strength (B_0) perpendicular to the flow direction is studied. The mathematical calculation of the Bejan number is under consideration. Herein, two scenarios are investigated: the first is the Couette flow and in the second scenario, both porous surfaces are parallel and fixed at a distance of $2h$, and the motion is a Poiseuille flow controlled by pressure. The flow across the x-axis is supposed to be generated and dependent on y exclusively. The governed system is solved using analytical solutions.

2 Entropy formation

Every thermodynamic system experiences entropy formation. The formation of entropy is directly linked to thermal irreversibility. It is crucial to find the rate of entropy formation in a framework to maximise the energy for the system's proper performance. Consider the motion of a Newtonian, incompressible fluid subject to the Fourier law of thermal conduction. The volumetric rate of entropy formation is expressed in a Cartesian pattern by Bejan [29,30] as

$$E_{\mathrm{G}} = \left\{ \begin{array}{c} \dfrac{\kappa}{T_0^2}\left[\left(\dfrac{\partial T}{\partial x^*}\right)^2 + \left(\dfrac{\partial T}{\partial y^*}\right)^2\right] + \dfrac{\mu}{T_0}\left[2\left[\left(\dfrac{\partial u^*}{\partial x^*}\right)^2 + \left(\dfrac{\partial v^*}{\partial y^*}\right)^2\right]\right. \\ \left. + \left[\left(\dfrac{\partial u^*}{\partial y^*}\right) + \left(\dfrac{\partial v^*}{\partial x^*}\right)\right]^2\right] + \dfrac{\sigma B_0^2}{T_0}(u^{*2} + v^{*2}) \end{array} \right\}. \quad (1)$$

A thermal or velocity differential is maintained in a system, and the preceding version of entropy formation

demonstrates that irreversibility is caused by conductivity (κ), viscous dissipation, and Ohmic heating.

In numerous significant convective thermal transport scenarios, velocity and temperature patterns are rationalized under the assumption that the flow is hydrodynamically evolving ($\frac{\partial v^*}{\partial x^*} = \frac{\partial u^*}{\partial x^*} = \frac{\partial v^*}{\partial y^*} = 0$), thermally advancing ($\frac{\partial T}{\partial x^*} \neq 0$), or thermally growing ($\frac{\partial T}{\partial x^*} = 0$) [31,32].

Eq. (1) is simplified to

$$E_G = \frac{\kappa}{T_0^2}\left(\frac{\partial T}{\partial y^*}\right)^2 + \frac{\mu}{T_0}\left(\frac{\partial u^*}{\partial y^*}\right)^2 + \frac{\sigma B_0^2}{T_0}u^{*2}. \tag{2}$$

By utilizing dimensionless quantities, Eq. (2) can be written as

$$N_s = \left(\frac{\partial \theta}{\partial y}\right)^2 + \frac{\mathrm{Br}}{\Omega}\left(\frac{\partial u}{\partial y}\right)^2 + \frac{M\mathrm{Br}}{\Omega}u^2 = N_t + N_f + N_m. \tag{3}$$

In the above equation, $N_s\left(=\frac{E_G T_0^2 h^2}{k(T_w - T_0)^2}\right)$ is the total entropy rate, $\alpha_1\left(\frac{T_w - T_0}{T_0}\right)$ is the temperature difference variable, and $\mathrm{Br}\left(=\frac{\mu U^2}{k(T_w - T_0)}\right)$ is the Brinkman number. Here, N_t is the thermal transport irreversibility, N_f is the fluid friction irreversibility, and N_m is the Joule heating irreversibility.

3 Bejan number

The Bejan number Be is an alternate dispersion criterion for irreversibility and signifies the ratio between the thermal transport irreversibility (N_t) and total irreversibility (N_s).

Therefore, the Bejan number can be determined using the computational model:

$$\mathrm{Be} = \frac{N_t}{N_s}, \tag{4}$$

or

$$\mathrm{Be} = \frac{\left(\frac{\partial \theta}{\partial y}\right)^2}{\left(\frac{\partial \theta}{\partial y}\right)^2 + \frac{\mathrm{Br}}{\Omega}\left(\frac{\partial u}{\partial y}\right)^2 + \frac{M\mathrm{Br}}{\Omega}u^2}. \tag{5}$$

The Bejan number ranges from 0 to 1. If Be = 1, the entropy is formed exclusively by the irreversibility of thermal transmission. If Be = 0, the total entropy is formed exclusively by the irreversibility of fluid friction, and if Be = 0.5, the total entropy is formed by the irreversibility of thermal transmission and friction. In this investigation, the second rule of thermodynamics is applied along with two simultaneous porous surfaces. In addition, two distinct scenarios are identified and analysed: the Couette flow with porous walls and the Poiseuille flow (pressure-driven) in a channel having viscous dissipation.

4 Mathematical derivation

Consider the constant flow of a viscous, electrically conducting, and compressible fluid in pathways made of two infinitely equivalent permeable surfaces divided by a length h. The x-axis extends in the flow path along the bottom stationary plate, whereas the y-axis is orthogonal to the surfaces. The channel plates are subjected to a consistent transverse magnetic field B_0 that is implemented perpendicularly. Herein, two scenarios are investigated: the first is the Couette flow, and in the second scenario, both porous surfaces are parallel and fixed at a distance of $2h$, and the motion is a Poiseuille flow controlled by pressure. The flow

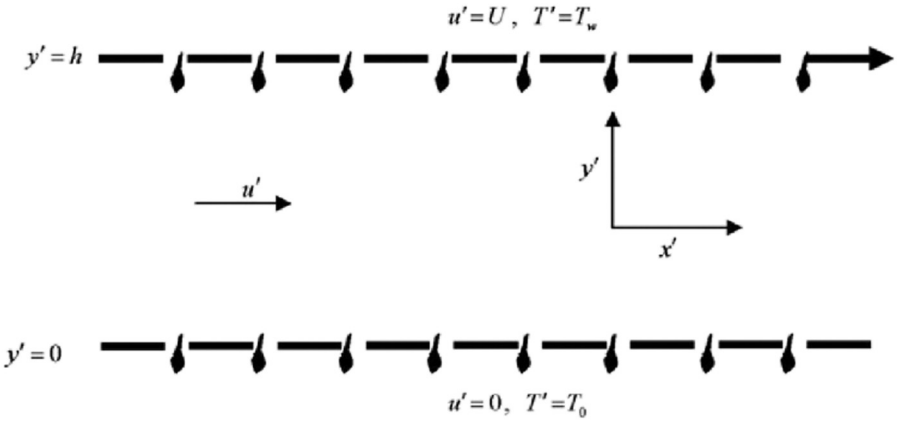

Figure 1: Couette flow involving suction/injection.

across the x-axis is supposed to be generated and dependent on y exclusively. We have the velocity component as $v = -v_0$, which corresponds to the suction/injection velocity. The Couette flow involving suction/injection is displayed in Figure 1.

The equations regulating the independent flow of a viscous, incompressible fluid are as follows:

4.1 Case 1: Couette flow

$$\nu\frac{d^2u^*}{dy^{*2}} + v_0\frac{du^*}{dy^*} - \frac{\sigma B_0^2}{\rho}u^* = 0, \tag{6}$$

$$\frac{k^*}{\rho C_p}\frac{d^2T^*}{dy^{*2}} + v_0\frac{dT^*}{dy^*} + \frac{\mu}{\rho C_p}\left(\frac{du^*}{dy^*}\right)^2 = 0. \tag{7}$$

The constraints include

$$\left.\begin{aligned} u^* = 0, T^* = T_0 \text{ at } y^* = 0 \\ u^* = U, T^* = T_w \text{ at } y^* = h \end{aligned}\right\}. \tag{8}$$

4.2 Solution of the problem (Case 1)

The following are the dimensionless components in the preceding computations:

$$y = \frac{y^*}{h}, S = \frac{v_0 h}{\nu}, u = \frac{u^*}{U}, M = \frac{\sigma B_0^2 h^2}{\rho\gamma}, \Pr = \frac{\mu C_p}{k},$$
$$\theta = \frac{T^* - T_0}{T_w - T_0} \text{ and } \mathrm{Ec} = \frac{U^2}{C_p(T_w - T_0)}.$$

Eqs. (6) and (7) are shown in dimensionless forms as

$$\frac{d^2u}{dy^2} + S\frac{du}{dy} - Mu = 0, \tag{9}$$

$$\frac{d^2\theta}{dy^2} + S\Pr\frac{d\theta}{dy} + \mathrm{Ec}\Pr\left(\frac{du}{dy}\right)^2 = 0, \tag{10}$$

with boundary conditions

$$\left.\begin{aligned} u = 0,\ \theta = 0 \text{ at } y = 0 \\ u = 1,\ \theta = 1 \text{ at } y = 1 \end{aligned}\right\}. \tag{11}$$

Solving Eqs. (9) and (10) subject to the boundary conditions (11), we obtain

$$u = C_1e^{\alpha y} + C_2e^{\beta y}, \tag{12}$$

where $\alpha, \beta = \frac{1}{2}\left[-s \pm (s^2 + 4M)^{\frac{1}{2}}\right]$,

$$\theta = D_1 + D_2e^{-s\Pr y} - \mathrm{Br}[C_3e^{2\alpha y} + C_4e^{2\beta y} + C_5e^{(\alpha+\beta)y}]. \tag{13}$$

4.3 Case 2: pressure-driven Poiseuille flow

The Poiseuille flow configuration with suction/injection is depicted in Figure 2.

The governing momentum and energy equation are as follows:

$$\nu\frac{d^2u^*}{dy^{*2}} + v_0\frac{du^*}{dy^*} - \frac{1}{\rho}\frac{dp}{dx} - \frac{\sigma B_0^2}{\rho}u^* = 0, \tag{14}$$

$$\frac{k^*}{\rho C_p}\frac{d^2T^*}{dy^{*2}} + v_0\frac{dT^*}{dy^*} + \frac{\mu}{\rho C_p}\left(\frac{du^*}{dy^*}\right)^2 = 0. \tag{15}$$

The boundary conditions are as follows:

$$\left.\begin{aligned} u^* = 0,\ T^* = T_w \text{ at } y^* = h \\ u^* = 0,\ T^* = T_0 \text{ at } y^* = -h \end{aligned}\right\}. \tag{16}$$

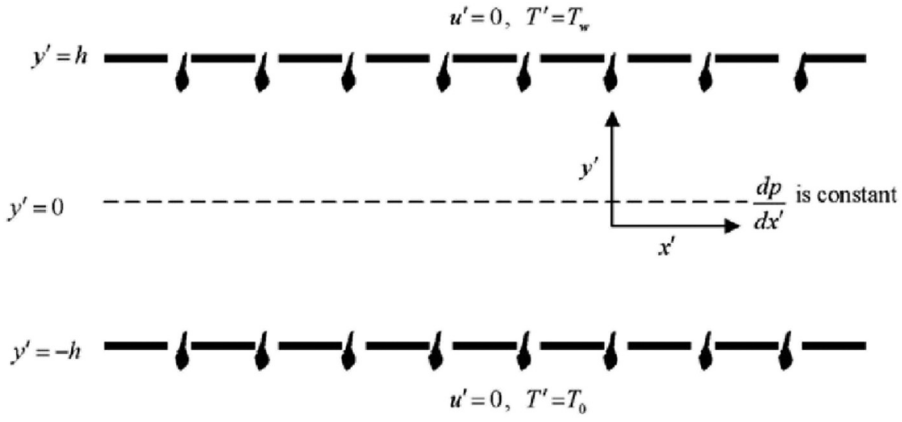

Figure 2: Pressure-compelled movement with suction/injection.

4.4 Solution of the problem (Case 2)

Eqs. (14) and (15) can be written as

$$\frac{d^2u}{dy^2} + s\frac{du}{dy} - Mu = 0, \tag{17}$$

$$\frac{d^2\theta}{dy^2} + s\mathrm{Pr}\frac{d\theta}{dy} + \mathrm{EcPr}\left(\frac{du}{dy}\right)^2 = 0, \tag{18}$$

with boundary conditions,

$$\left.\begin{aligned} u = 0,\ \theta = 1 \text{ at } y = 1 \\ u = 0,\ \theta = 0 \text{ at } y = -1 \end{aligned}\right\}. \tag{19}$$

Solving Eqs. (17) and (18) subject to (19) gives

$$u = K_1 e^{\alpha y} + K_2 e^{\beta y} + \frac{1}{M}, \tag{20}$$

where

$$\alpha, \beta = \frac{1}{2}\left[-S \pm (S^2 + 4M)^{\frac{1}{2}}\right], \tag{21}$$

$$\theta = L_1 + L_2 e^{-s\mathrm{Pr}y} - \mathrm{Br}[K_3 e^{2\alpha y} + K_4 e^{2\beta y} + K_5 e^{(\alpha+\beta)y}]. \tag{22}$$

5 Validation of results

Table 1 is constructed for verification of the accuracy of the present analysis. Here, we examined the comparative analysis of heat transport rates for the Prandtl number (Pr) with those of Ahmed *et al.* [33]. Clearly, one can notice that the results are in an outstanding agreement.

6 Results and discussion

Entropy formation on magnetohydrodynamics in a channel with suction/suction is examined in this section. In both instances, the figures illustrate the impact of a non-dimensional governing attribute on velocity, temperature, Bejan number, and entropy formation. Various flow characteristics are depicted in Figures 3–18 for the first case, in which the

Table 1: Comparison of the thermal transport rates with those of Ahmed *et al.* [33]

Pr	Ahmed *et al.* [33]	Present results
0.2	0.231	0.23102
0.6	0.347	0.34716
1.2	0.521	0.52135

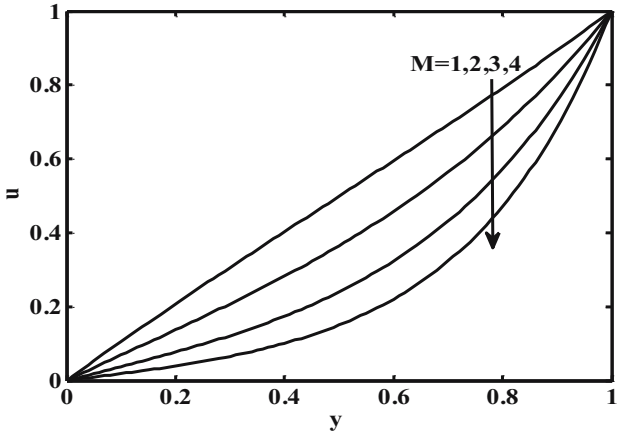

Figure 3: Case 1: velocity *versus* magnetic parameter M when S = 0.5.

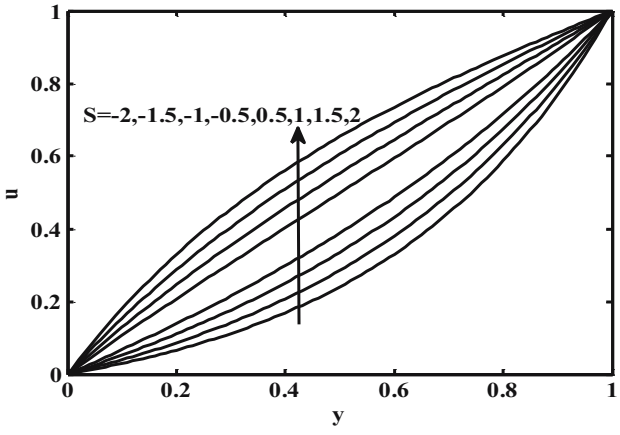

Figure 4: Case 1: velocity *versus* suction/injection parameter S when M = 1.

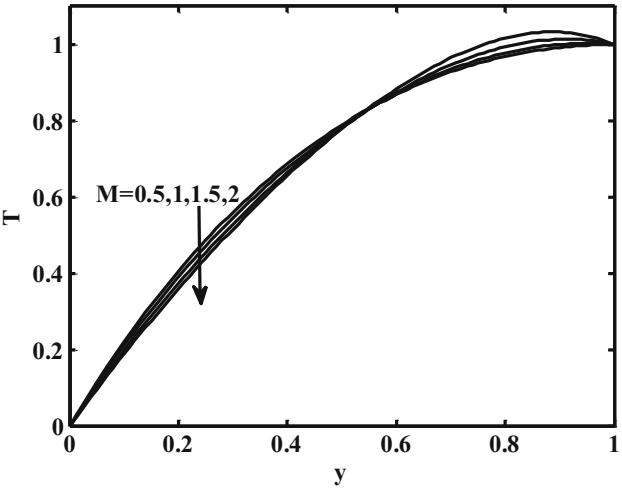

Figure 5: Case 1: temperature *versus* magnetic parameter M when S = 0.5, Br = 2, and Pr = 0.71.

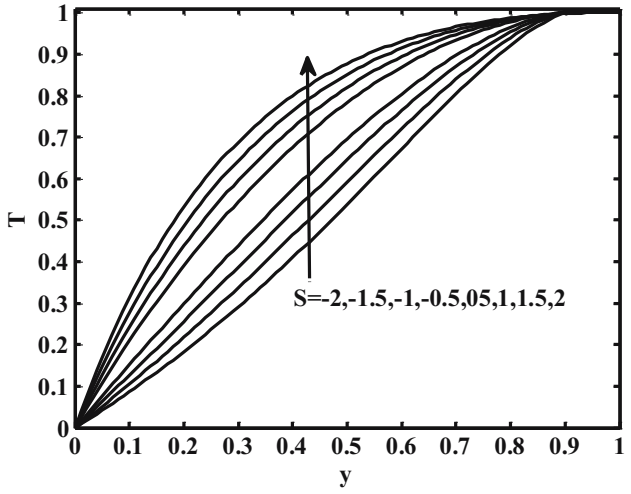

Figure 6: Case 1: temperature *versus* suction/injection parameter S when M = 1, Br = 2, and Pr = 0.71.

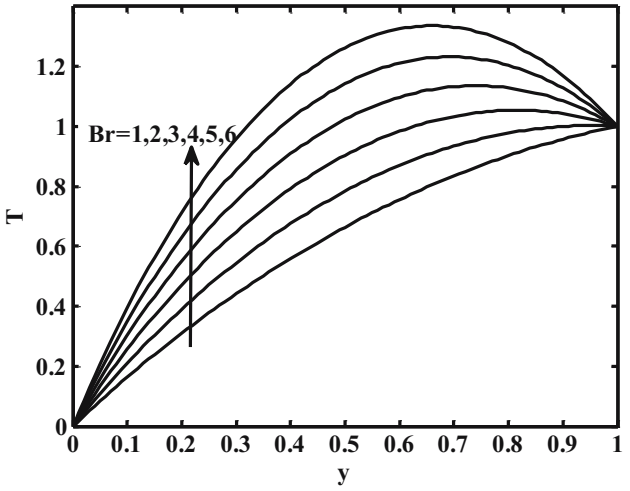

Figure 8: Case 1: temperature *versus* Brinkman number Br when M = 1, S = 0.5, and Pr = 0.71.

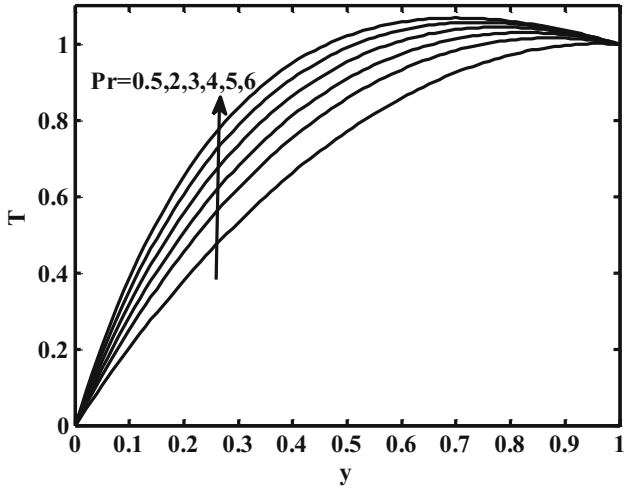

Figure 7: Case 1: temperature *versus* Prandtl number Pr when M = 1, Br = 2, and S = 0.5.

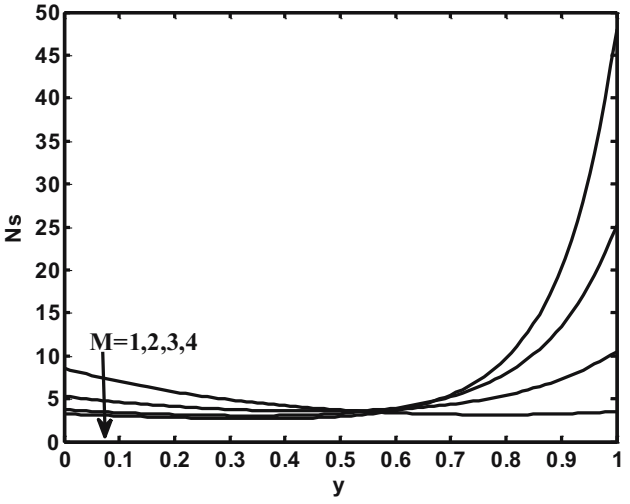

Figure 9: Case 1: entropy formation number N_s *versus* M when S = 0.5, Br = 2, Pr = 0.71, and $Br\Omega^{-1}$ = 1.

flow is situated between a migrating and a fixed porous plate, and in Figures 19–34 for the second scenario, in which the flow is between two parallel stable porous plates attributable to a pressure gradient.

6.1 Case 1: couette flow

As illustrated in Figures 3 and 5, the effect of the magnetic field strength M on the velocity and temperature is that the velocity decreases as M increases. This decrease is caused by the effect of Lorentz force acting as a resistance to flow as expected. As shown in Figure 5, the temperature θ decreases with an increase in M. The decrease is attributed to the Lorentz force acting as friction to the intended motion. As shown in Figure 5, the temperature θ decreases as M increases.

The impacts of the suction/injection S on the velocity u and temperature θ are depicted in Figures 4 and 6. We found that both the velocity and the temperature increase as S increases. This is true at a physical level, as the fluid suction improves with fluid velocity, hence boosting shearing heating inside the channel. The figures show the temperature fluctuation for various Prandtl numbers. It is evident that the temperature of a fluid increases as the volume increases. As a result of this improvement in the Prandtl number, the thermal diffusivity of the conducting fluid drops, resulting in a reduction in the heat created by viscous dissipation

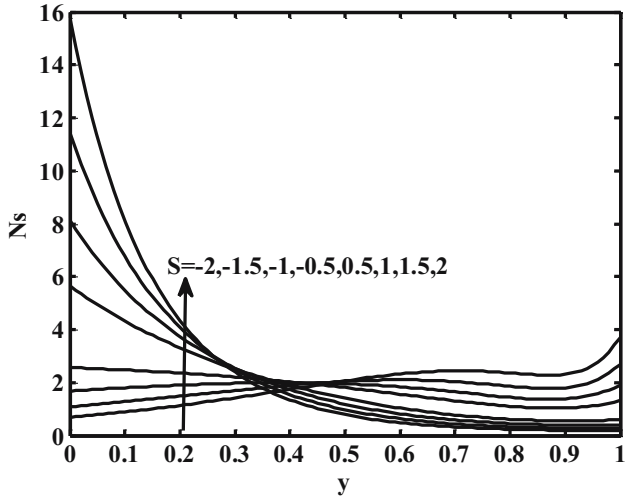

Figure 10: Case 1: entropy formation number N_s *versus* S when M = 1, Br = 2, Pr = 0.71, and $Br\Omega^{-1}$ = 1.

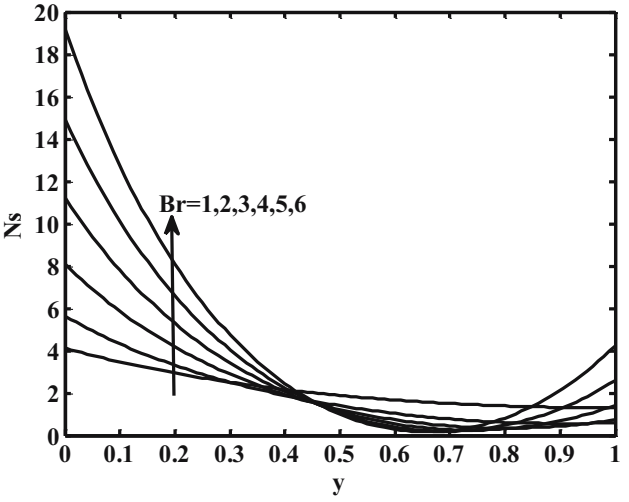

Figure 12: Case 1: entropy formation number N_s *versus* Br when M = 1, Pr = 0.71, S = 0.5, and $Br\Omega^{-1}$ = 1.

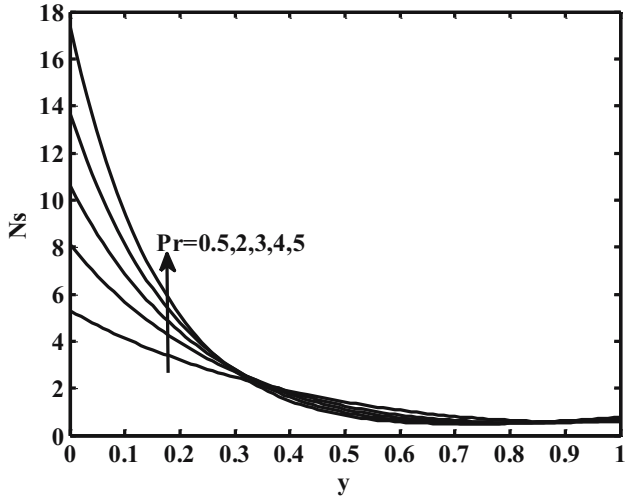

Figure 11: Case 1: entropy formation number N_s *versus* Pr when M = 1, Br = 2, S = 0.5, and $Br\Omega^{-1}$ = 1.

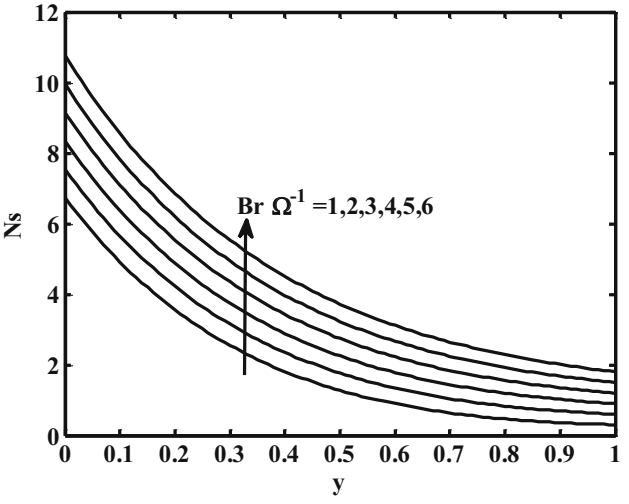

Figure 13: Case 1: entropy formation number N_s *versus* $Br\Omega^{-1}$ when M = 1, Pr = 0.71, S = 0.5, and Br = 2.

inside the channel. Figures 7 and 8 illustrate the changes in the temperature for distinct Prandtl and Brinkman numbers. This is because as the Brinkman number increases, the viscous dissipation within the channel becomes more pronounced, causing the temperature to also increase.

Figures 9–13 show the effects of the various regulating factors on the entropy formation N_s inside the channel. The magnetic field characteristic M on the entropy formation N_s decreases with increasing M attributes at the wall at y = 1 and has the reverse pattern at y = 0. According to Figure 10, the influence of the suction/injection component S on the entropy N_s is within the channel. It is shown that the entropy formation improves with suction (+S) but decreases with injection (+I) near a cooled, static porous plate (–S). Near the advancing hot porous plate, the opposite trend can be noticed. The significance of the Prandtl number Pr on the entropy formation inside the channel is depicted in Figure 11. It indicates that N_s increases as Pr increases. As Pr increases, the temperature gradient widens with improvement. Figures 12 and 13 illustrate the impact of the Brinkman number on the entropy formation.

We noticed that N_s grows as Br improves. Around the channel surfaces, the impact of Br on entropy formation is more significant but it decreases towards the midline from both permeable plates. It has been found that there is a fluid region inside the channel wherein Br has no effect on

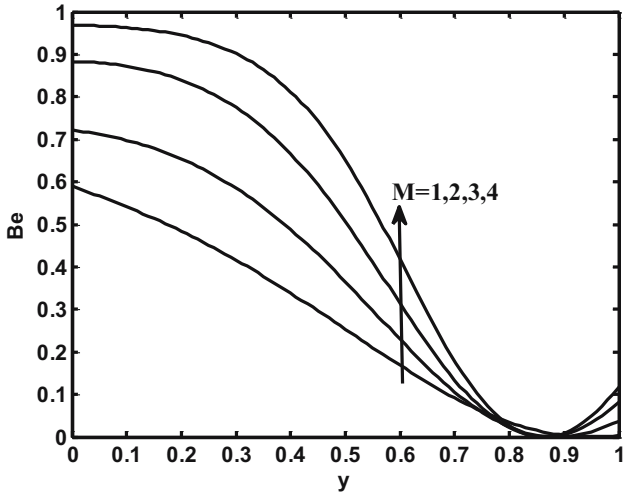

Figure 14: Case 1: Bejan number *versus* M when, S = 0.5, Pr = 0.71, Br = 2, and $\mathrm{Br}\Omega^{-1}$ = 1.

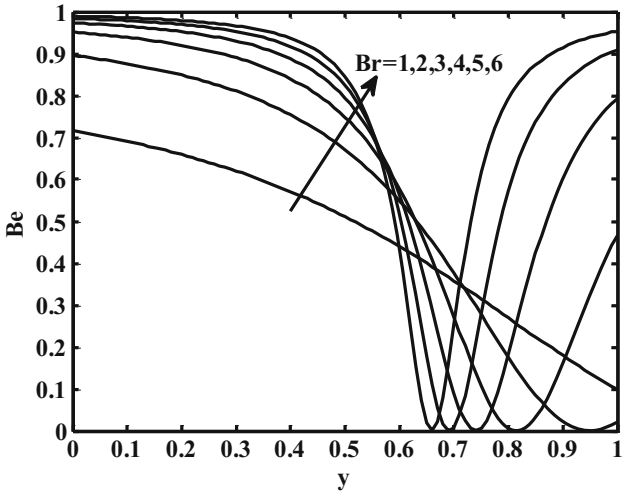

Figure 17: Case 1: Bejan number *versus* Br when M = 1, S = 0.5, Pr = 0.71, and $\mathrm{Br}\Omega^{-1}$ = 1.

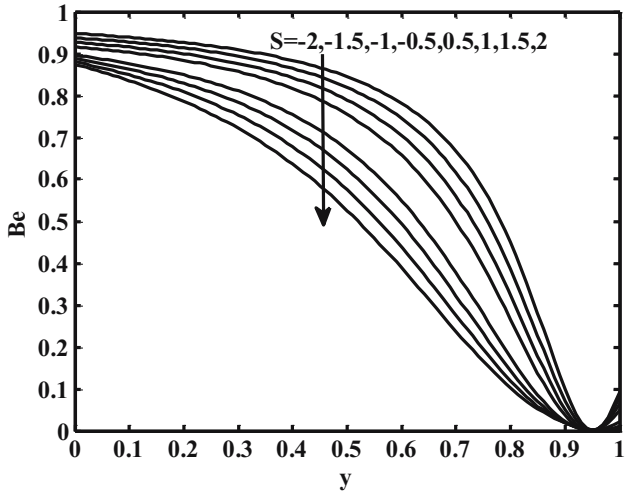

Figure 15: Case 1: Bejan number *versus* S when, M = 1, Pr = 0.71, Br = 2, and $\mathrm{Br}\Omega^{-1}$ = 1.

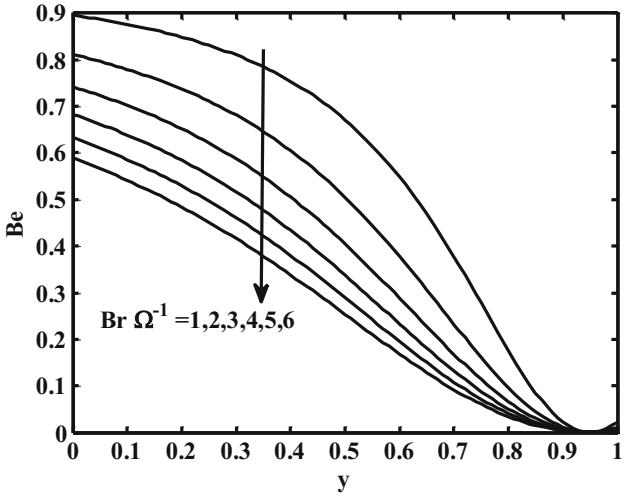

Figure 18: Case 1: Bejan number *versus* $\mathrm{Br}\Omega^{-1}$ when M = 1, S = 0.5, Pr = 0.71, and Br = 2.

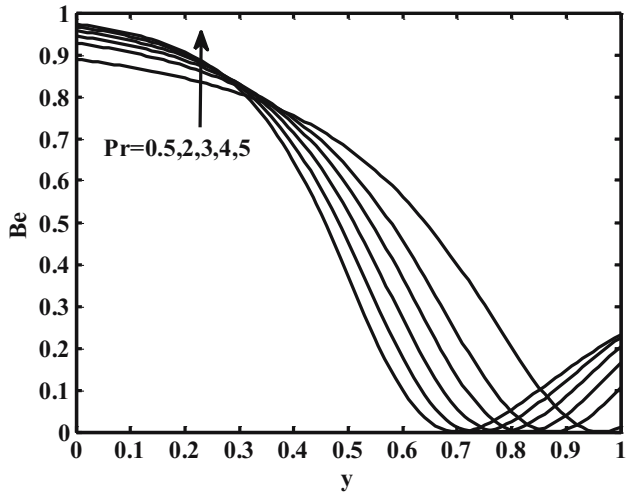

Figure 16: Case 1: Bejan number *versus* Pr when M = 1, S = 0.5, Br = 2, and $\mathrm{Br}\Omega^{-1}$ = 1.

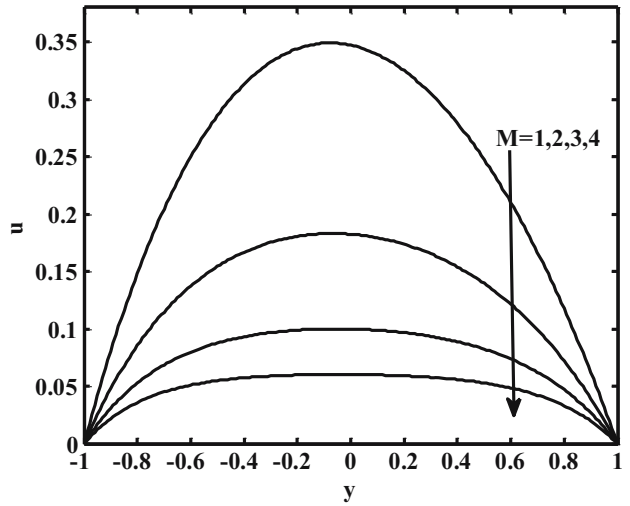

Figure 19: Case 2: velocity *versus* magnetic parameter M when S = 0.5.

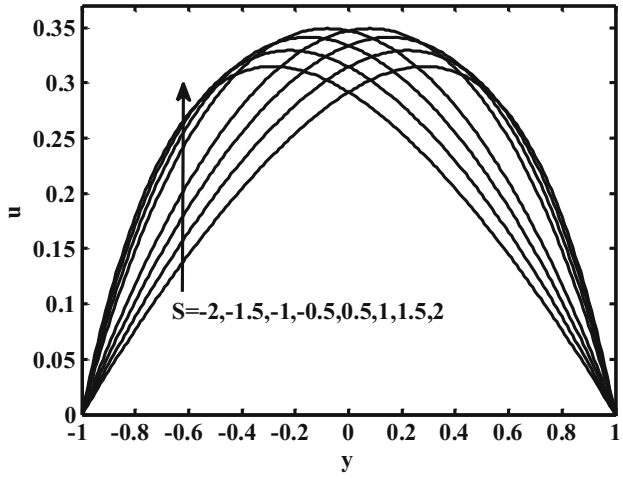

Figure 20: Case 2: velocity *versus* suction/injection parameter S when M = 1.

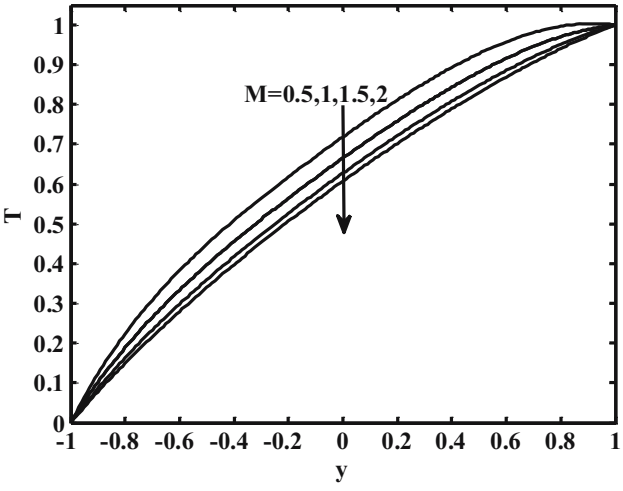

Figure 21: Case 2: temperature *versus* magnetic parameter M when S = 0.5, Br = 2, and Pr = 0.71.

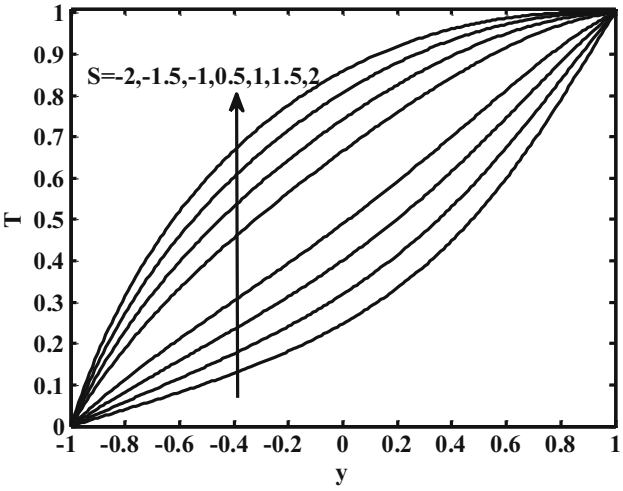

Figure 22: Case 2: temperature *versus* suction/injection parameter S when M = 1, Br = 2, and Pr = 0.71.

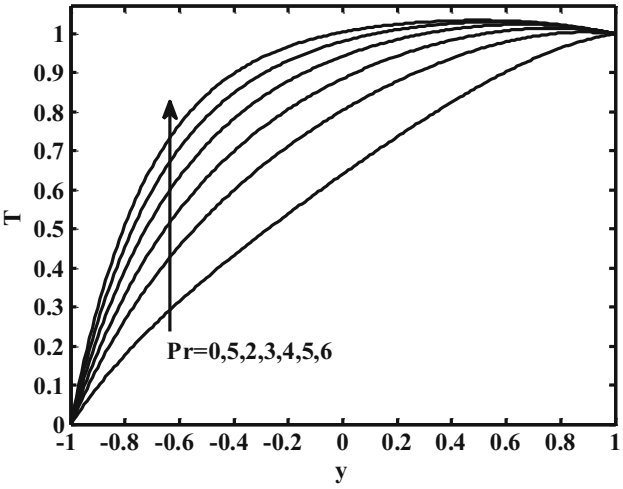

Figure 23: Case 2: temperature *versus* Prandtl number Pr when M = 1, Br = 2, and S = 0.5.

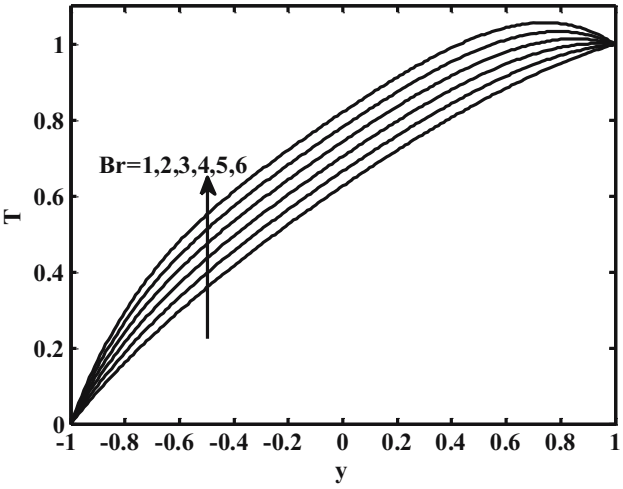

Figure 24: Case 2: temperature *versus* Brinkman number Br when M = 1, S = 0.5, and Pr = 0.71.

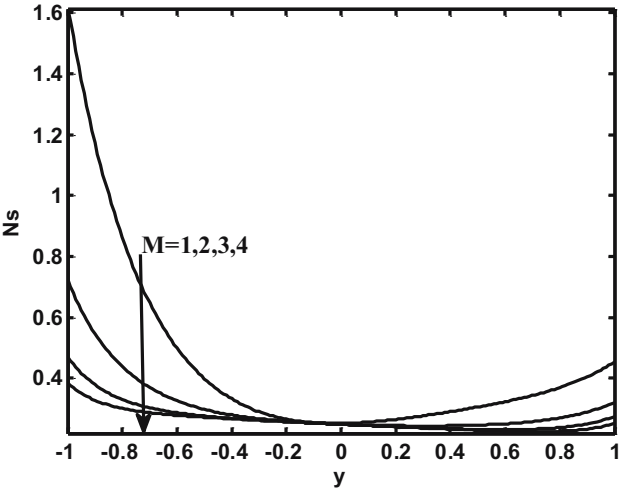

Figure 25: Case 2: entropy formation number N_s *versus* M when S = 0.5, Br = 2, Pr = 0.71, and $Br\Omega^{-1}$ = 1.

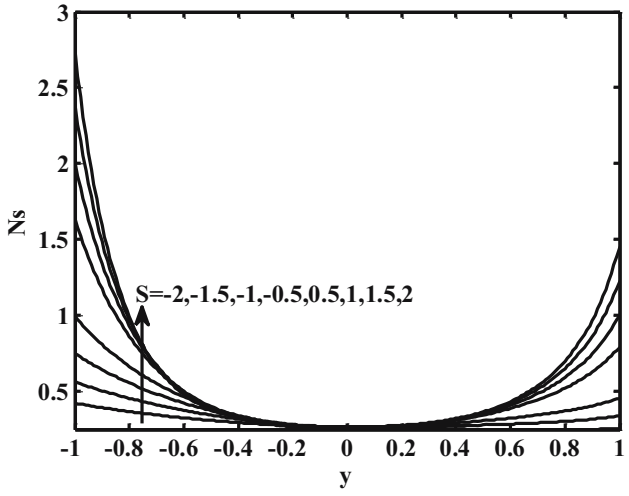

Figure 26: Case 2: entropy formation number N_s *versus* S when M = 1, Br = 2, Pr = 0.71, and $Br\Omega^{-1}$ = 1.

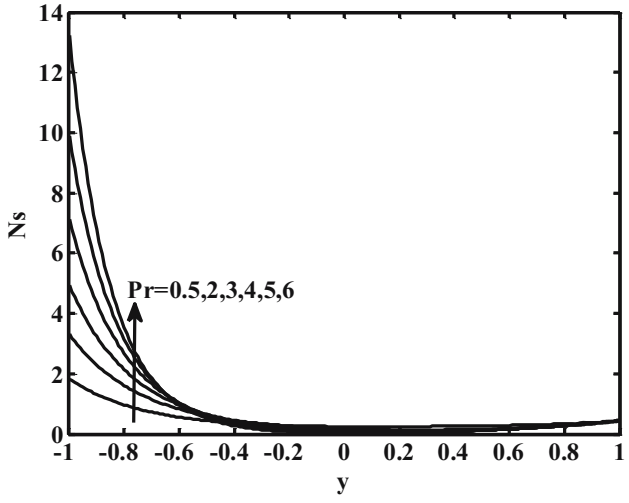

Figure 27: Case 2: entropy formation number N_s *versus* Pr when M = 1, Br = 2, S = 0.5, and $Br\Omega^{-1}$ = 1.

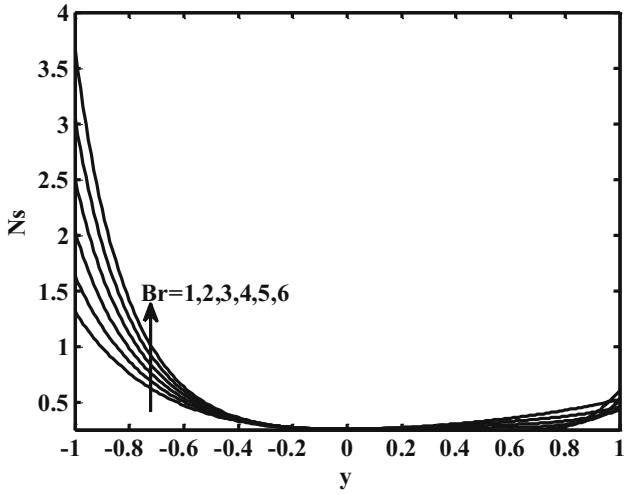

Figure 28: Case 2: entropy formation number N_s *versus* Br when M = 1, Pr = 0.71, S = 0.5, and $Br\Omega^{-1}$ = 1.

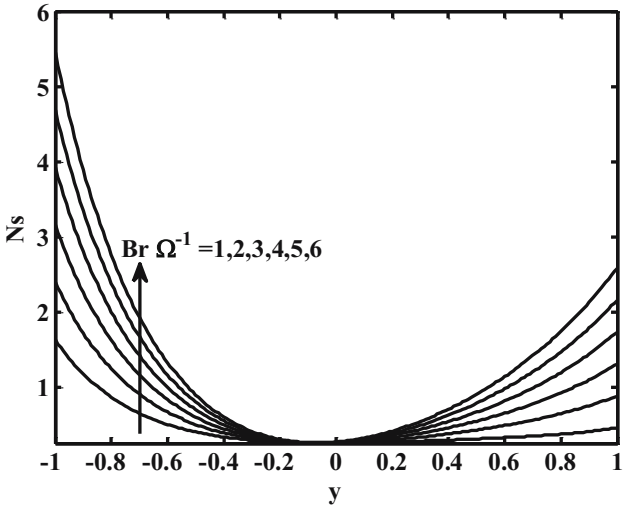

Figure 29: Case 2: entropy formation number N_s *versus* $Br\Omega^{-1}$ when M = 1, Pr = 0.71, S = 0.5, and Br = 2.

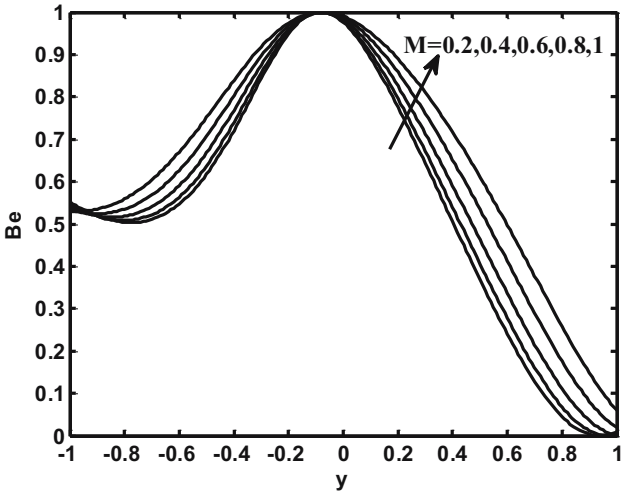

Figure 30: Case 2: Bejan number *versus* M when S = 0.5, Pr = 0.71, Br = 2, and $Br\Omega^{-1}$ = 1.

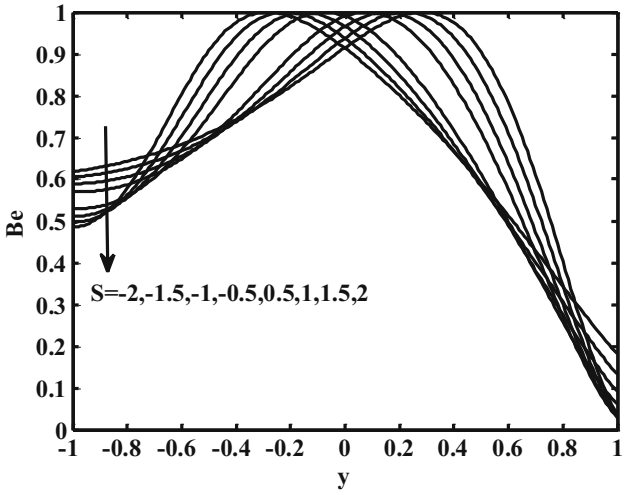

Figure 31: Case 2: Bejan number *versus* S when M = 1, Pr = 0.71, Br = 2, and $Br\Omega^{-1}$ = 1.

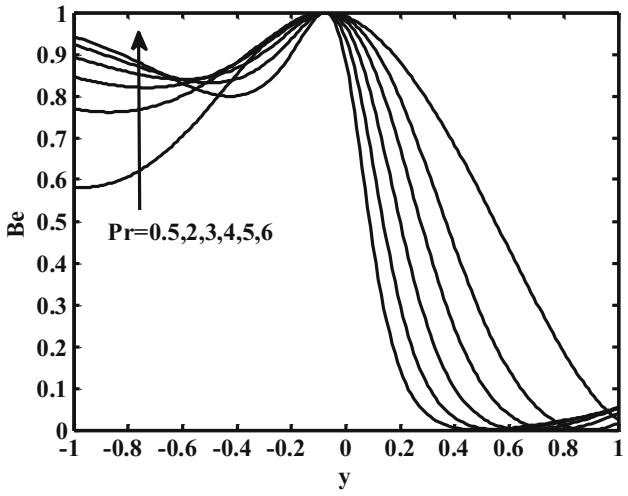

Figure 32: Case 2: Bejan number *versus* Pr when M = 1, S = 0.5, Br = 2, and $\mathrm{Br}\Omega^{-1}$ = 1.

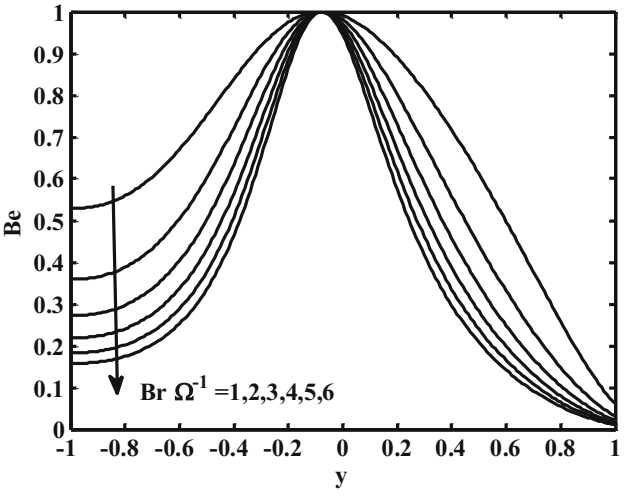

Figure 34: Case 2: Bejan number *versus* $\mathrm{Br}\Omega^{-1}$ when M = 1, S = 0.5, Pr = 0.71, and Br = 2.

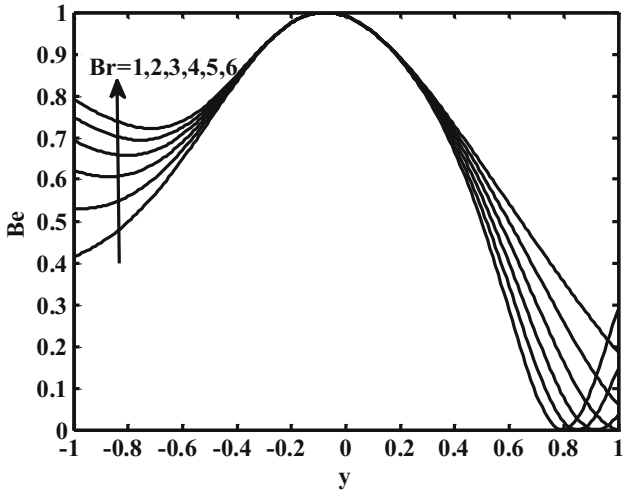

Figure 33: Case 2: Bejan number *versus* Brwhen M = 1, S = 0.5, Pr = 0.71, and $\mathrm{Br}\Omega^{-1}$ = 1.

the entropy. According to Figure 14, the effect of increasing the magnetic field M on the Bejan number Be increases, while the effect of increasing the suction/injection component S values on Bejan number Be decreases, as shown in Figure 15. Figures 16–18 depict the proportion of heat transport irreversibility to the total entropy formation. Around the cold, static porous plate, the thermal performance irreversibility promotes entropy formation, whereas, around the hot, circulating porous plate, the fluid friction irreversibility is the primary contributor. As Pr increases, it is noticed that the effect of heat transport irreversibility increases near the cold static porous plate, while the effect of fluid friction irreversibility reduces near the hot conveying porous plate. Near the centreline of the channel, the strength of fluid friction irreversibility on entropy formation is seen to increase as the Prandtl number increases. For all settings of the group characteristics, fluid friction irreversibility leads the entropy formation close to the heated, moving porous surface. In Figure 17, the Bejan tnumber corresponds to various values of the Brinkman

Table 2: Couette motion: numerical values of the skin friction coefficient for different values of the magnetic parameter M and S at y = 0

S/M	Skin friction C_f			
	1	2	3	4
−2	0.2689	0.1779	0.0987	0.0491
−1	0.4964	0.3235	0.1766	0.0868
0	0.8509	0.5514	0.2995	0.1466
1	1.3495	0.8793	0.4802	0.2361
2	1.9866	1.3143	0.7290	0.3631

Table 3: Pressure-driven Poiseuille flow: numerical values of the skin friction coefficient for different values of the magnetic parameter M and $S$with y = 0

S/M	Skin friction C_f			
	1	2	3	4
−2	0.1505	0.0605	0.0205	0.0067
−1	0.0935	0.0342	0.0109	0.0034
1	−0.0935	−0.0342	−0.0109	−0.0034
2	−0.1505	−0.0605	−0.0205	−0.0067

Table 4: Couette motion: numerical values of Nusselt number for different values of the magnetic parameter M and S with Br = 0.5, Pr = 0.71, and y = 0.1

S/M	$\theta^1(0)$				$\theta'(1)$			
	1	2	3	4	1	2	3	4
−2	0.8097	0.7628	0.7323	0.7171	0.5931	1.2060	2.0524	2.9959
−1	1.2482	1.1450	1.0868	1.0637	0.3509	0.9543	1.8121	2.7729
1	2.6786	2.2933	2.1048	2.0540	0.0681	0.5348	1.3062	2.2249
2	3.7027	3.0702	2.7578	2.6797	0.0155	0.3843	1.0656	1.9226

Table 5: Pressure-driven Poiseuille flow: numerical values of Nusselt number for different values of the magnetic parameter M and $S$with Br = 0.5, Pr = 0.71, and y = 0.1

S/M	$\theta'(0)$				$\theta'(1)$			
	1	2	3	4	1	2	3	4
−2	0.3766	0.3676	0.3653	0.3648	−1.0030	−1.3468	−1.4543	−1.4862
−1	0.4670	0.4621	0.4608	0.4605	−0.4834	−0.8015	−0.8914	−0.9176
1	0.4537	0.4585	0.4599	0.4602	−0.0135	−0.1546	−0.1991	−0.2138
2	0.3525	0.3615	0.3638	0.3643	0.0277	−0.0413	−0.0680	−0.0781

number. For comparatively small quantities of Br, the thermal performance irreversibility promotes entropy formation around the cold static porous plate, but the fluid friction irreversibility leads from the centreline to the hot flowing porous plate. For significant Br numbers, irreversible thermal expansion controls the entropy formation close to both channel permeable plates. Furthermore, Figure 17 demonstrates that when the Brinkman number increases, the majority of heat transport irreversibility near the porous plates increases efficiency, while the effect of fluid friction irreversibility around the centreline also increases. In this figure, there is a fluid area inside the channel wherein Br has no influence. Both heat transport and fluid friction directly contribute to the overall entropy formation (Be = 0.5) at the specified region.

Figure 18 depicts the spatial patterns of the Bejan number inside the channel for varying values of the group characteristics ($\mathrm{Br}\Omega^{-1}$). It illustrates that for comparatively small ranges of ($\mathrm{Br}\Omega^{-1}$), heat transport irreversibility leads to entropy formation close to the cold, static porous surface (y = 1), but as ($\mathrm{Br}\Omega^{-1}$)improves, the thermal performance irreversibility eventually yields to fluid friction irreversibility.

6.2 Case 2: pressure-driven Poiseuille flow

Figures 19 and 21 illustrate the effect of the magnetic field component M on the velocity u and temperature T patterns. With increasing magnetic field configuration M, a behaviour equivalent to that of Couette flow (Case 1) is

Table 6: Couette motion: numerical values of Nusselt number for different values of Brinkman number Br and Prandtl number Pr with S = 0.5, M = 1, and y = 0.1

Br/Pr	$\theta'(0)$				$\theta'(1)$			
	2	3	4	5	2	3	4	5
1	2.1609	2.5471	2.9643	3.4069	−0.1595	−0.0458	0.0370	0.0944
2	2.7397	3.1634	3.6156	4.0902	0.2629	0.3392	0.3871	0.4124
3	3.3186	3.7798	4.2668	4.7735	0.6854	0.7242	0.7371	0.7305
4	3.8975	4.3961	4.9181	5.4568	1.1078	1.1092	1.0872	1.0485

Table 7: Pressure-driven Poiseuille flow: numerical values of Nusselt number for different values of Brinkman number *Br* and Prandtl number Pr with $S = 0.5$, $M = 1$, and $y = 0.1$

Br/*Pr*	$\theta'(0)$				$\theta'(1)$			
	2	3	4	5	2	3	4	5
1	0.4199	0.3449	0.2677	0.1988	−0.0376	0.0277	0.0583	0.0697
2	0.4143	0.3376	0.2597	0.1909	0.0814	0.1341	0.1539	0.1563
3	0.4087	0.3302	0.2517	0.1831	0.2004	0.2404	0.2496	0.2430
4	0.4032	0.3229	0.2438	0.1753	0.3193	0.3468	0.3452	0.3296

observed, while the reverse behaviour is observed for temperature variation T.

Figures 20 and 22 illustrate the effect of the suction/injection component on the velocity and temperature and were similar to that of the Couette flow (Case 1). That is, the velocity and temperature improve as the suction/injection component S increases. Figures 23, 27 and 32 depict the influence of the Prandtl number Pr on the temperature, entropy formation proportion N_s, and Bejan number Be. With an increase in the Prandtl number Pr, the temperature, entropy formation number N_s, and Bejan number Be are shown to increase. The effect of the Prandtl number on temperature is identical to that of the Couette flow (Case 1). We have observed that the thermal performance irreversibility outperforms the entropy formation near a cold porous plate, whereas the fluid friction irreversibility prevails near a warm porous plate. As Pr increases, it is observed that the effect of heat transport irreversibility around the cold porous plate increases, whereas the effect of the fluid friction irreversibility around the hot porous plate is not affected by changes in Pr. As Pr approaches close to the centreline, the participation of the thermal performance irreversibility to the total entropy formation decreases.

Figures 24, 28 and 33 illustrate the effect of the Brinkman number Br on the temperature, entropy formation number N_s, and Bejan number Be. The temperature, entropy formation number N_s, and Bejan number Be have all been found to increase when Br increases. The fact that the temperature increases as Br increases is analogous to the Couette flow (Case 1). We noticed that as Br increases, the entropy formation due to the irreversibility of fluid friction improves. Therefore, as Br increases, the temperature gradient around the cold porous surface develops.

Figures 25 and 26 depict the effects of the magnetic field component M and suction/injection quantity S on the entropy formation number N_s. The entropy regime decreases with an increase in M and the opposite behaviour in N_s is observed with an increase in S. From Figure 25, we can see that the flow is slowed down by the magnetic field's transverse application, and Ohmic dissipation causes a significant temperature increase in the porous channel as M increases. Figure 26 demonstrates that it increases the impacts of S. On the cold porous plate, we noticed that the N_s increases with increasing suction (+S) but decreases with increasing injection (–S). We differ with the fact that the N_s is greater in the Couette flow (Figure 10) than in the pressure-driven flow (Figure 25).

Figures 29–31 show the behaviour of $\mathrm{Br}\Omega^{-1}$, the magnetic parameter (M), and the suction/injection parameter (S) on the entropy formation and Bejan number, respectively. Here, we have noticed from these figures that the entropy rate and Bejan number curves are increased against increasing estimations of the magnetic parameter and $\mathrm{Br}\Omega^{-1}$.But an opposite behaviour is noticed for the suction/injection parameter on the Bejan number.

The calculated values of the coefficient for skin friction C_f with velocity for Couette mobility and pressure-driven Poiseuille are provided in Tables 2 and 3 for a variety of suction parameters (S) and Hartmann number M variables.

According to Table 2, the coefficient for skin friction C_f increases as the suction parameter S increases and falls as the Hartmann number M increases for Couette mobility. The coefficient of skin friction C_f decreases as the suction parameter S and Hartmann number M increase in Table 3 for pressure-driven Poiseuille flow.

Tables 4 and 5 list the calculated values of the thermal transfer rates $\theta'(0)$ and $-\theta'(1)$ for various values of the suction parameter S and the Hartmann number M. It is noticed from Table 4 that the heat transport rate $\theta'(0)$ and $-\theta'(1)$ decrease as the suction parameter $S = -1, -2$ and the Hartmann number M increase, while the converse occurs as the rotation parameter K^2 increases. This is reasonable from a scientific standpoint. With increasing values of the rotational factor, the viscous fluid is heated quickly, and as a result, the rate of heat transfer between the surfaces increases.

Tables 4–7 give the rate of heat transmission coefficients $\theta'(0)$ and $-\theta'(1)$ for varying values of suction/injection component, magnetic field component, Brinkman number, and Peclet number. According to Table 4, the suction/injection

component increases the heat transfer rate at plate $y = 0$ but decreases at plate $y = 1$.

However, we found a complete reversal in the upward trend of magnetic field input variables. Table 5 demonstrates that the suction/injection clearly shows the heat transmission rate at both surfaces, but the magnetic field component minimizes. The Brinkman number and Peclet number increase the heat transmission rate at both surfaces in Couette circulation, as shown in Table 6. Moreover, Table 7 reveals that both the Brinkman number and the Peclet number decrease the heat transmission rate at the surface $y = 0$, whereas the opposite is true at the surface $y = 1$.

The Be matching to various Br values is shown in Figure 34. We noticed that transmission irreversibility outperforms entropy formation close to the cold porous plate, with an outright increase occurring around the centre of the channel. From the centreline towards the hot porous plate, the fluid friction irreversibility is controlled, and as the porous plate is reached, the thermal performance irreversibility becomes dominant only at huge Br attributes.

7 Conclusions

To design and control pipelines or procedure apparatus, understanding the flow regime is important since significant flow features, for example, average and unstable pressure drop, the steadiness of throughput, and homogeneity of wall refrigerating or heating fluctuate prominently depending upon the flow regime. Unfortunately, the forecast of the flow regime is a challenging problem that has not yet been solved. The governing system is solved analytically. The main conclusions are the following:

- Entropy formation is greater near the cloud porous plate in contrast to the hot porous plate.
- The escalating values of the suction/injection parameter increase the fluid temperature.
- The increase in the magnetic field parameter decreases the momentum boundary layer.
- The Brinkman number improves the thermal boundary thickness.
- The magnetic field parameter, suction/injection, and Brinkman number increase the entropy formation in both cases.
- An increase in the Brinkman number and magnetic field parameter improves the entropy formation.

Acknowledgments: Researchers Supporting Project number (RSPD2023R576), King Saud University, Riyadh, Saudi Arabia.

Funding information: This project was funded by King Saud University, Riyadh, Saudi Arabia. This work is supported by the Doctoral Startup Foundation of Shandong Technology and Business University (No. BS202306).

Author contributions: All authors have accepted responsibility for the entire content of this manuscript and approved its submission.

Conflict of interest: The authors state no conflict of interest.

References

[1] Muhuri PK. Effect of rotation on unsteady hydro magnetic Couette flow. J Phys Soc Jpn. 1963;18:1671.
[2] Hartmann J, Lazarus F. Kongelige danske videnskabernes selskab, Matematisk-Fysiske Meddelelser, Vol. 15; 1937. p. 6–7. View at Google Scholar.
[3] Sutton GW, Sherman A. Engineering Magnetohydrodynamics. New York: McGraw Hill; 1965.
[4] Y Liu, L Zheng, X Zhang. Unsteady MHD Couette flow of a generalized Oldroyd-B fluid with fractional derivative. Comput Math Appl. 2011;61:443–50.
[5] Rahbari A, Abbasi M, Rahimipetroudi I, Sundén B, Ganji DD, Gholami M. Heat transfer and MHD flow of non-Newtonian Maxwell fluid through a parallel plate channel: analytical and numerical solution. Mech Sci. 2018;9:61–70.
[6] Dawar A, Thumm T, Islam S, Shah Z. Optimization of response function on hydromagnetic buoyancy-driven rotating flow considering particle diameter and interfacial layer effects: Homotopy and sensitivity analysis. Int Commun Heat Mass Transf. 2023;144:106770. doi: 10.1016/j.icheatmasstransfer.2023.106770.
[7] Dawar A, Islam S, Shah Z, Mahmuod SR. A passive control of Casson hybrid nanofluid flow over a curved surface with alumina and copper nanomaterials: A study on sodium alginate-based fluid. J Mol Liq. 2023;382:122018. doi: 10.1016/j.molliq.2023.122018.
[8] Wood LC. Thermodynamics of Fluid Systems. Oxford, UK: Oxford University Press; 1975.
[9] Ibanez G, Cuevas S, Haro MLD. Minimization of entropy generation by asymmetric convective cooling. Int J Heat Mass Transf. 2003;46:1321–8.
[10] Mahmud S, Fraser RA. Flow, thermal, and entropy generation characteristics inside a porous channel with viscous dissipation. Int J Therm Sci. 2005;44:21–32.
[11] Makinde OD, Eegunjobi AS. Effects of convective heating on entropy generation rate in a channel with permeable Walls. Entropy. 2013;15:220–33.
[12] Eegunjobi AS, Makinde OD. Effects of Navier slip on entropy generation in a porous channel with suction/injection. J Therm Sci Technol. 2012;7:522–35.
[13] Zhao C, Cheung CF, Xu P. High-efficiency sub-microscale uncertainty measurement method using pattern recognition. ISA Trans. 2020;101:503–14.

[14] Dai B, Zhang B, Niu Z, Feng Y, Liu Y, Fan Y. A novel ultrawideband branch waveguide coupler with low amplitude imbalance. IEEE Trans Microw Theory Tech. 2020;70(8):1–9. doi: 10.1109/TMTT.2022.3186326.
[15] Xu K, Guo Y, Liu Y, Deng X, Chen Q, Ma Z. 60-GHz compact dual-mode on-chip bandpass filter using GaAs technology. IEEE Electron Device Lett. 2021;42(8):1120–3.
[16] Du S, Xie H, Yin J, Fang T, Zhang S, Sun Y, Zheng R. Competition pathways of energy relaxation of hot electrons through coupling with optical, surface, and acoustic phonons. J Phys Chem C. 2023;127(4):1929–36.
[17] Wang Y, Lou M, Wang Y, Fan C, Tian C, Qi X. Experimental investigation of the effect of rotation rate and current speed on the dynamic response of riserless rotating drill string. Ocean Eng. 2023;280:114542.
[18] Khan SA, Razaq A, Alsaedi A, Hayat T. Modified thermal and solutal fluxes through convective flow of Reiner-Rivlin material. Energy. 2023;283:128516. doi: 10.1016/j.energy.2023.128516.
[19] Singh K, Pandey AK, Kumar M. Numerical solution of micropolar fluid flow via stretchable surface with chemical reaction and melting heat transfer using Keller-Box method, propulsion and power. Research. 2021;10:194–207.
[20] Xu YJ, Khan SA, Khan MI, Alzahrani F, Bafakeeh OT. Irreversibility analysis in time-dependent Darcy–Forchheimer flow of viscous fluid with diffusion-thermo and thermo-diffusion effects. Open Phys. 2022;20:875–87. doi: 10.1515/phys-2022-0136.
[21] Eegunjobi AS, Makinde OD. Entropy generation analysis in a variable viscosity MHD channel flow with permeable walls and convective heating. Math Probl Eng. 2013;2013:630798.
[22] Chauhan DS, Rastogi P. Radiation effects on natural convection MHD flow in a rotating vertical porous channel partially filled with a porous medium. Appl Math Sci. 2010;4:643–55.
[23] Vyas P, Srivastava N. Radiative MHD flow over a non-isothermal stretching sheet in a porous medium. Appl Math Sci. 2010;4:2475–84.
[24] Manglesh A, Gorla MG. MHD free convective flow through porous medium in the presence of hall current, radiation and thermal diffusion. Ind J Pure Appl Math. 2013;44:743–56.
[25] Kumar V, Jain S, Sharma K, Sharma P. Entropy generation in Poiseuille flow through a channel partially filled with a porous material. Theor Appl Mech. 2015;42(1):35–51.
[26] Chauhan DS, Khemchandani V. Entropy generation in the Poiseuille flow of a Temperature dependent viscosity fluid through a channel with a naturally permeable wall under thermal radiation. Adv Appl Sci Res. 2016;7(4):104–20.
[27] Das S, Jana RN. Entropy generation in MHD porous channel flow under constant pressure gradient. Appl Maths Phys. 2013;1(3):78–89.
[28] Vyas P, Rai A. Entropy regime for radiative MHD couette flow inside a channel with naturally permeable base. Int J Energy Technol. 2013;5(19):1–9.
[29] Bejan A. A study of entropy generation in fundamental convective heat transfer. Trans ASME J Heat Transf. 1979;101:718–25.
[30] Bejan A. Convection Heat Transfer. New York: John Wiley & Sons; 1984.
[31] Burmeister LC. Convective Heat Transfer. New York: Wiley; 1993.
[32] White FM. Viscous Fluid Flow. New York: McGraw-Hill; 1974.
[33] Ahmed I, Alghamdi M, Amjad M, Aziz F, Akbar T, Muhammad T. Numerical investigation of MHD flow of hyperbolic tangent nanofluid over a non-linear stretching sheet. Heliyon. 2023;9:e17658. doi: 10.1016/j.heliyon.2023.e17658.

Appendix

$$C_1 = \frac{1}{[e^{\alpha} - e^{\beta}]}, C_2 = \frac{-1}{[e^{\alpha} - e^{\beta}]},$$

$$C_3 = \frac{\alpha^2 C_1{}^2}{4\alpha^2 + 2s\mathrm{Pr}\alpha}, C_4 = \frac{\beta^2 C_2{}^2}{4\beta^2 + 2s\mathrm{Pr}\beta}, C_5 = \frac{2\alpha\beta C_1 C_2}{(\alpha+\beta)^2 + s\mathrm{Pr}(\alpha+\beta)},$$

$$C_6 = C_3 + C_4 + C_5, C_7 = C_3 e^{2\alpha} + C_4 e^{2\beta} + C_5 e^{\alpha+\beta},$$

$$D_1 = \frac{1 - \mathrm{Br}(e^{-s\mathrm{Pr}} C_6 - C_7)}{1 - e^{-s\mathrm{Pr}}}, D_2 = \frac{-1 + \mathrm{Br}(C_6 - C_7)}{1 - e^{-s\mathrm{Pr}}},$$

$$K_1 = \frac{\sinh\beta}{M\sinh(\alpha-\beta)}, K_2 = \frac{-\sinh\alpha}{M\sinh(\alpha-\beta)},$$

$$K_3 = \frac{\alpha^2 K_1{}^2}{4\alpha^2 + 2s\mathrm{Pr}\alpha}, K_4 = \frac{\beta^2 K_2{}^2}{4\beta^2 + 2s\mathrm{Pr}\beta}, K_5 = \frac{2\alpha\beta K_1 K_2}{(\alpha+\beta)^2 + s\mathrm{Pr}(\alpha+\beta)},$$

$$C_6 = C_3 + C_4 + C_5, C_7 = C_3 e^{2\alpha} + C_4 e^{2\beta} + C_5 e^{\alpha+\beta},$$

$$L_2 = \frac{1 - 2\mathrm{Br}[K_3 \sinh 2\alpha + K_4 \sinh 2\beta + K_5 \sinh 2(\alpha+\beta)]}{2\sinh(s\mathrm{Pr})},$$

$$L_1 = -L_2 e^{s\mathrm{Pr}} + \mathrm{Br}[K_3 e^{-2\alpha y} + K_4 e^{-2\beta y} + K_5 e^{-(\alpha+\beta)y}].$$